Ray Contribution Masks for Structure Adaptive Sinogram Filtering

Michael Balda, Joachim Hornegger and Bjoern Heismann

***Abstract*—The patient dose in CT imaging is linked to measurement noise. Various noise-reduction techniques have been developed that adapt structure preserving filters like anisotropic diffusion or bilateral filters to CT noise properties. We introduce a structure adaptive sinogram (SAS) filter that incorporates the specific properties of the CT measurement process. It uses a point-based forward projector to generate a local structure representation called Ray Contribution Mask (RCM). The similarities between neighboring RCMs are used in an enhanced variant of the bilateral filtering concept, where the photometric similarity is replaced with the structural similarity. We evaluate the performance in four different scenarios: The robustness against reconstruction artifacts is demonstrated by a scan of a high-resolution-phantom. Without changing the modulation transfer function (MTF) nor introducing artifacts, the SAS filter reduces the noise level by 13.6 %. The image sharpness and noise reduction capabilities are visually assessed on in-vivo patient scans and quantitatively evaluated on a simulated phantom. Unlike a standard bilateral filter, the SAS filter preserves edge information and high-frequency components of organ textures well. It shows a homogeneous noise reduction behavior throughout the whole frequency range. The last scenario uses a simulated edge phantom to estimate the filter MTF for various contrasts: The noise reduction for the simple edge phantom exceeds 80 %. For low contrasts at 55 Hounsfield units (HU), the mid-frequency range is slightly attenuated, at higher contrasts of approx. 100 HU and above, the MTF is fully preserved.**

***Index Terms*—Computed Tomography, noise reduction, nonlinear filters, dose reduction.**

I. Introduction

CT image quality is predominantly influenced by the signal to noise ratio (SNR) and the image modulation transfer function (MTF). Noise reduction techniques are an essential tool in medical CT as image noise greatly influences the detectability of details in a reconstructed CT volume and thus its diagnostic value. As the most dominant noise component in CT, quantum noise, is directly related to detected X-ray intensity, successful noise reduction leads to a reduction of patient X-ray dose [1].

In general, dose efficiency of CT acquisitions is driven by several means including dynamic exposure control [2], tube filters like the wedge filter [3] and optimized detector designs that maximize the Detective Quantum Efficiency (DQE) [4]–[7]. For filtered back projection (FBP)-based reconstructions [8], [9], projection- or image-domain filters are applied to reduce the required patient dose. The most common filtering strategy applied in medical CT scanners consists in modifying the high-pass reconstruction kernel used for FBP in a way that high frequencies are less amplified or blocked [10]. For most diagnostic tasks, the relevant information is supposed to be primarily contained in the lower-frequency components of the image. Each CT manufacturer offers a broad spectrum of task-specific reconstruction kernels that block irrelevant frequency components and consequently noise.

More advanced noise reduction techniques use adaptive filters. This type of filters steers the filter strength according to a noise estimate and causes less smoothing in regions where noise is low, i.e. the X-ray intensity is less attenuated. For instance, an adaptive filter for reducing noise induced streak artifacts in very strongly attenuated data is shown in [11]. Kachelrieß et al. [12] have introduced an adaptive filter that is applied in projection domain and features non-linear filtering in channel, projection and z-direction for various types of projection data such as helical cone-beam CT. In [13], a method for wavelet-based denoising of projection data is introduced. This approach is especially suited for dual source data [14] with similar tube-voltage settings for two low-dose data-sets. It utilizes the noise correlations between the two aligned data-sets to construct an adaptive wavelet-based filter.

Well-known edge preserving filters have also been investigated. Edge-preserving anisotropic diffusion filters [15], [16] can be adapted to CT data as shown in [17]. The purpose of this filter is to smooth along but not across edges. It relies on gradient information and noise can deteriorate the edge information and erroneously preserve noise-induced structures. As a consequence true edges are weakened or false ones are enhanced. This problem has to be avoided by carefully choosing the smoothing parameters for the gradient estimation based on local noise estimates. Schaap et al. [18] have developed an image-based fast denoising method based on anisotropic diffusion. This method features an adapted diffusion filter to preserve small structures.

Bilateral filtering [19] tries to achieve a similar goal by combining spatial- and intensity-based smoothing. This filter type steers the smoothing locally according to distance and similarity of neighboring intensity values. In CT, frequency-based noise reduction filters are usually applied in the projection domain as the spectral noise properties in the CT-image or -volume domain can hardly be derived analytically. The image noise is inhomogeneous and non-stationary and

Manuscript received November 7, 2011.

M. Balda is with the Metrilus GmbH, Erlangen, Germany and with the Pattern Recognition Lab, Friedrich-Alexander-University Erlangen Nuremberg, Germany. E-mail: michael.balda@metrilus.de.

J. Hornegger is with the Pattern Recognition Lab, Friedrich-Alexander-University Erlangen Nuremberg, Germany.

B. Heismann is with Siemens Healthcare, Erlangen, Germany and with the Pattern Recognition Lab, Friedrich-Alexander-University Erlangen Nuremberg, Germany.

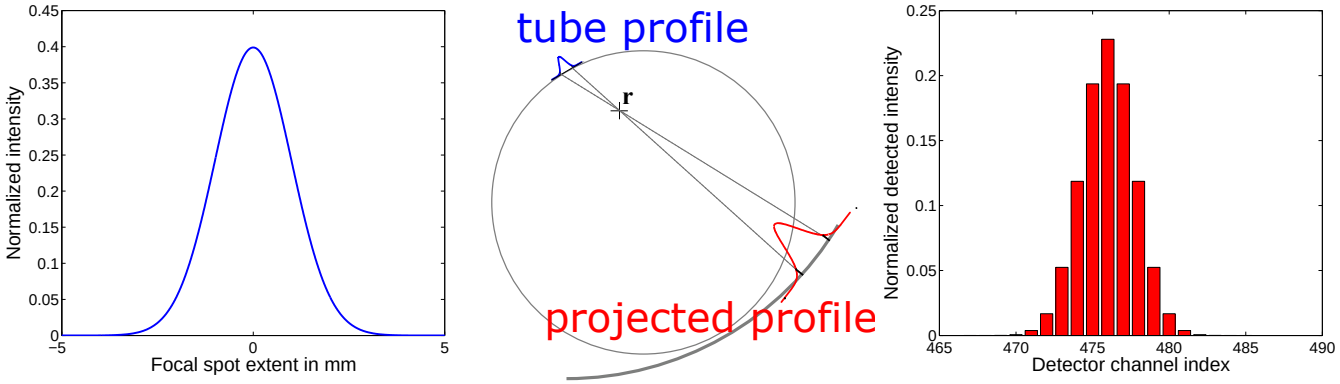

(a) Normally distributed tube-profile. (b) Schematics of projection process. (c) Sampled projected tube-profile $\bar{\mu}_{\mathrm{L}}(c, r_1)$ for fixed projection p_1.

Fig. 1. Illustration of the working principle of the projection operator $\mathcal{P}_{\mathrm{P}}(\mathbf{r}, \bar{\mu}(\mathbf{r}))$. A complete result of $\mathcal{P}_{\mathrm{P}}(\mathbf{r}, \bar{\mu}(\mathbf{r}))$ is displayed in Fig. 2.

estimating local noise properties is complex, for instance Borsdorf et al. [20] demonstrate how to estimate local variance and analyze noise correlations in the image domain for CT-data reconstructed with indirect FBP. Manducha et al. [21] introduced a noise-adaptive bilateral filter on projection data where the photometric similarity is computed on an estimate of the actual quantum numbers.

All of these strategies have one common goal: Reducing the noise level of the reconstructed images while maintaining a desired level of image sharpness and details.

CT noise-reduction filters can be divided into two main categories: Pre- and post-reconstruction filters. Pre-reconstruction filters like [11]–[13], [17], [21] are applied to the projection data. The FBP filter-kernel described in [9] is usually used as a simple pre-reconstruction kernel to steer the trade-off between noise suppression and image sharpness. The advantage of filtering in this domain is the simplicity of the noise characteristics: In the projection-space, the noise is almost white, only minor noise correlations are introduced by the detection process, for instance due to the optical crosstalk of scintillators [22]. These effects have minor influence and usually can be neglected when designing noise-reduction filters. Additionally, the magnitude of the noise can easily be estimated from the measured attenuation values which allows for noise adaption of the filter. Edge-preserving pre-reconstruction filters are, however, limited by the inferior contrast-to-noise ratio in sinogram space. Low-contrast structures in the imaged object can hardly be identified in projection space due to the noise in CT projections at standard dose levels. Additionally the contrast and CNR level even of homogeneous structures varies throughout the projections. Non-linear edge-preserving filters may not be able to preserve those structures throughout the whole sinogram which generally leads to a loss in sharpness. It also may cause inconsistencies in the projection data which results in artifacts in the reconstructed image. Consequently, pre-reconstruction filters may deal with noise properties well, but have a weakness in recognizing the structure of the signal.

Post-reconstruction filters such as [18], [23]–[25] operate on reconstructed images and thus cannot produce or intensify reconstruction artifacts. However, the noise properties are much more complicated in the reconstructed image as most reconstruction steps introduce noise correlations by filtering and interpolation [20]. Furthermore, the structure and the local magnitude of the noise is dependent on the whole object instead of merely the local attenuation. As a consequence, edge-preserving frequency-based post-reconstruction filters need to model the projection noise and measurement noise and the whole reconstruction process.

We introduce an Structure Adaptive Sinogram (SAS) filter that operates in the projection domain and uses a projection model to recover local structures in the projection space from a pre-reconstructed image. It yields an individual local filter kernel for each measurement value. This local kernel adapts its smoothing directions to the local structures, thus the projection noise level can be strongly reduced while the sharpness of low-contrast structures can be preserved. It basically uses two parameters which allow steering its filter strength and smoothing properties so it can be adapted to the demands of specific diagnostic tasks. The filter is an extension of the bilateral filter [19]. It replaces the photometric similarity measure with a more robust, CT-specific structural similarity term. It incorporates the measurement process by using a point-based projector and a pre-reconstructed image. The filter itself is not noise adaptive, but can be combined with projection-domain noise adaption techniques such as [21] which steer the filter accordingly.

II. Theory

The SAS filter uses a point-based forward projector to generate a local structure representation called Ray Contribution Mask (RCM). The similarities between neighboring RCMs are used to compute an individual, non-linear filter kernel for each projection value. Additionally, a RCM-driven range adaption is applied to avoid inconsistencies which may cause reconstruction artifacts.

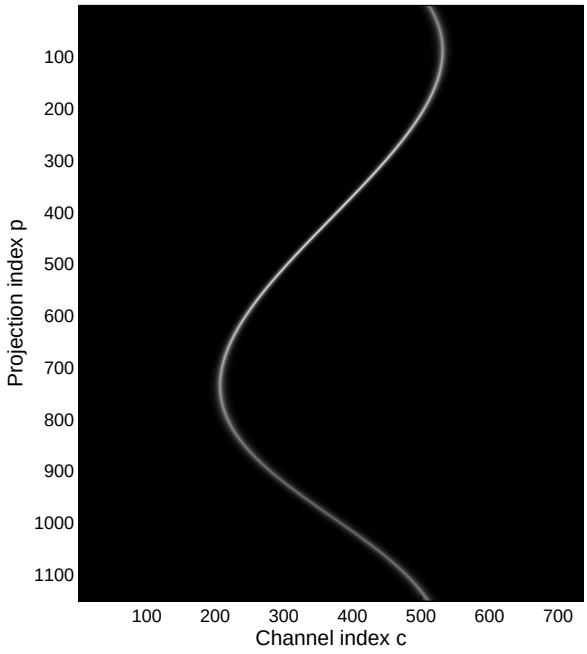

Fig. 2. Result of point-based projection operator for all channels and projections at a fixed location $\mathbf{r}$ (scale: arbitrary units). For visualization purposes, an extremely large X-ray focus of 9 mm full width-half maximum (FWHM) was used.

A. Point-Based Analytic Projection

In practice, CT projections deviate from the ideal line-projection model. This is for instance caused by sampling and discretization effects, finite focal spot sizes and detector cross-talk. We use a flexible model of the projection process called point-based analytic projection which can take into account these effects. We denote this single detector row variant $\mathcal{P}_{\mathrm{P}}(\mathbf{r}, \bar{\mu}(\mathbf{r}))$. The continuous 2-D function $\bar{\mu}(\mathbf{r})$ denotes the reconstructed attenuation values of a CT slice. This operator yields the contribution of a delta impulse at position $\mathbf{r}$ to the measured values at discrete channel indices $c \in \mathbb{Z}$ and line projections $p \in \mathbb{Z}$. It may include effects like the focus beam profile and size and detector channel characteristics. The projections p correspond to the sampled gantry angles ν, so $\nu = p \cdot \Delta\nu$ with the angular sample distance $\Delta\nu$. In a CT system, this sampling process features a temporal integration of the projections during the reading time. The function $\mathcal{P}_{\mathrm{P}}(\mathbf{r}, \bar{\mu}(\mathbf{r}))$ yields the information where the contributions from a single point in the object space appear in the sinogram.

Figure 1 illustrates an exemplatory output of the projection operator $\mathcal{P}_{\mathrm{P}}(\mathbf{r}, \bar{\mu}(\mathbf{r}))$ for a single gantry angle without temporal smearing of the projected tube profile. It features a normally distributed tube profile model (Fig. 1a), a geometric projection model (Fig. 1b) and a detection model (Fig. 1c). The latter may include detector pixel geometry, sampling properties like active pixel areas and detector cross talk. $\mathcal{P}_{\mathrm{P}}(\mathbf{r}, \bar{\mu}(\mathbf{r}))$ can be viewed as a transform that takes the function of local attenuation values in object space $\bar{\mu}(\mathbf{r})$ as an input and yields for a given location $\mathbf{r}$ all contributions of $\bar{\mu}(\mathbf{r})$ in projection space. Figure 2 depicts these contributions for a specific $\mathbf{r}$.

The simplest variant featuring ideal integration, no cross-talk and ideal temporal sampling reads:

$$\mathcal{P}_{\mathrm{P}}(\mathbf{r}, \bar{\mu}(\mathbf{r})) = \bar{\mu}(\mathbf{r}) \cdot \sum_{c'=-\infty}^{+\infty} \sqcap\left(\frac{\beta - c'\Delta\beta}{\Delta\beta}\right) * \mathcal{N}_p^{(\beta_{\mathbf{r},\nu}, \sigma^2_{\mathbf{r},\nu})}(\beta), \tag{1}$$

This equation models the sampling of a normally distributed, projected tube profile by the detector. The operator $*$ denotes the convolution. $\mathcal{N}_p^{(\beta_{\mathbf{r},\nu}, \sigma^2_{\mathbf{r},\nu})}(\beta)$ is the tube profile projected onto the detector for projection p. Its mean value $\beta_{\mathbf{r},\nu}$ is the detector channel angle corresponding to the location $\mathbf{r}$ and the gantry angle ν and its standard deviation $\sigma_{\mathbf{r},\nu}$ is the standard deviation of the tube profile σ_{T} times a stretch factor determined by the pinhole projection model indicated in Fig. 1b. $\Delta\beta$ is the fan angle between two channels, $\sqcap(\beta)$ is the rectangle function of width 1, centered at $\beta = 0$. The fan beam geometry is illustrated in Fig. 3.

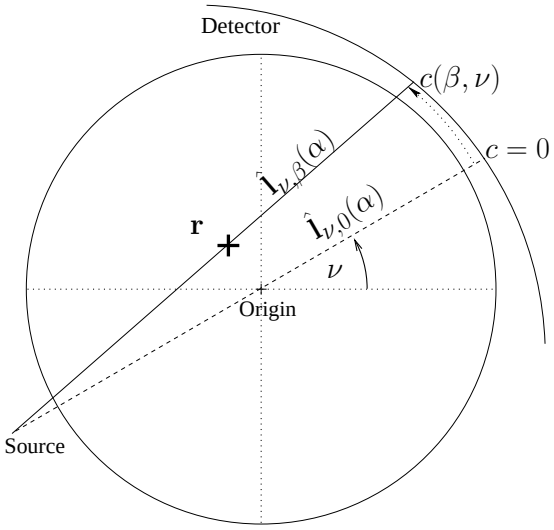

Fig. 3. Schematics and notation for fan-beam geometry.

For a source position $\mathbf{s}_\nu \in \mathbb{R}^2$ and a source-detector distance of d_{SD} we get the projected point location:

$$\mathbf{r}_{\mathrm{D},\nu} = \mathbf{s}_\nu + d_{\mathrm{SD}} \cdot \frac{(\mathbf{r} - \mathbf{s}_\nu)}{\|\mathbf{r} - \mathbf{s}_\nu\|_2}. \tag{2}$$

From this we can compute the corresponding channel angle $\beta_{\mathbf{r},\nu}$ with the rotated channel location $\mathbf{r}'_{\mathrm{D},\nu}$:

$$\mathbf{r}'_{\mathrm{D},\nu} = \mathbf{R}_{-\nu}\mathbf{r}_{\mathrm{D},\nu} + (d_{\mathrm{SD}}, 0)^T \tag{3}$$

$$\beta_{\mathbf{r},\nu} = \arctan_2(r'_{\mathrm{D},\nu,y}, r'_{\mathrm{D},\nu,x}) \tag{4}$$

with

$$\mathbf{r}'_{\mathrm{D},\nu} = (r'_{\mathrm{D},\nu,x}, r'_{\mathrm{D},\nu,y})^T \tag{5}$$

The function $\arctan_2$ is the well-known variation of the arctangent function for polar coordinate transforms and $\mathbf{R}_{-\nu}$ is the rotation matrix that rotates a point by $-\nu$.

The standard deviation $\sigma_{\mathbf{r},\nu,r}$ can be computed as follows:

$$\sigma_{\mathbf{r},\nu} = \frac{\|\mathbf{r}_{\mathrm{D},\nu} - \mathbf{r}\|_2}{\|\mathbf{s}_\nu - \mathbf{r}\|_2} \cdot \sigma_{\mathrm{T}} \tag{6}$$

B. Ray Contribution Masks

We use the point-based projection operator $\mathcal{P}_{\mathrm{P}}(\mathbf{r}, \bar{\mu}(\mathbf{r}))$ to calculate the contribution of a local measured value to its neighbors by sampling the projection ray that corresponds to the measured attenuation at $\hat{c}$, $\hat{p}$. A single point in the projection space approximately corresponds to a line in object space ($\hat{\mathbf{l}}_{\nu,\beta}(\alpha)$ in Fig. 3). See Figs. 4a – 4c for examples on a simple phantom. We sample this line at distinct locations indexed by k and call the sampled locations $\hat{\mathbf{r}}_{\hat{c},\hat{r},k}$. Then we compute all point-projections $\mathcal{P}_{\mathrm{P}}(\hat{\mathbf{r}}_{\hat{c},\hat{p},k}, \bar{\mu}(\hat{\mathbf{r}}_{\hat{c},\hat{p},k}))$ for the samples points on the line. The sum of all point-projections is the RCM $R_{\hat{c},\hat{p}}(c,p)$:

$$R_{\hat{c},\hat{p}}(c,p) = \sum_k \mathcal{P}_{\mathrm{P}}\left(\hat{\mathbf{r}}_{\hat{c},\hat{p},k}, \bar{\mu}(\hat{\mathbf{r}}_{\hat{c},\hat{p},k})\right) \tag{7}$$

It quantifies contributions of the projection line at $\hat{c}$, $\hat{p}$ to the complete sinogram. For sampling the projection line, we use a maximum sample distance of one pixel spacing in object space. Best results are achieved for sampling distances of approx. 0.75 to 1 pixel spacing. For larger sampling distances small image features could be missed. Smaller sampling distances do not contribute any additional information and would just slow down the computation.

The RCM drops very fast with respect to distance from the center position $(\hat{c},\hat{p})$ so in practice, it can be limited to a neighborhood of 5 to 11 projections. We call this parameter $\Delta p_{\max}$. The size limitation in terms of channels can be determined by computing the outmost non-zero points of the integrated projections.

In order to reduce the RCM to the most dominant structures, we neglect all ray samples for which $\bar{\mu}(\mathbf{r})$ falls below a given fraction p_{S} of the maximum attenuation value along the sampled ray, so $\hat{\mathbf{r}}_{\hat{c},\hat{p},k}$ includes only the samples above the scaled maximum value. This percentage is an important filter parameter which is called *structure preservation parameter* p_{s} consecutively. In practice, values in the range of $p_{\mathrm{s}} = 0.75$ to $p_{\mathrm{s}} = 0.95$ lead to best results.

Figure 4d shows an example of some RCMs with $\Delta p_{\max} = 7$ for different rays and different local structures. The projection line corresponding to example I intersects no specific dominant structures, so all $\mathcal{P}_{\mathrm{P}}\left(\hat{\mathbf{r}}_{\hat{c},\hat{p},k}, \bar{\mu}(\hat{\mathbf{r}}_{\hat{c},\hat{p},k})\right)$ have identical weights and the contributions of the water background are spread evenly on an hour-glass shape. Example II contains the small circle, which appears as a dominant structure, therefore the RCM consists mostly of the trajectory of this structure in the sinogram. Example III contains two dominant structures at very different image locations. These appear as two trajectories in the RCM.

C. Structural Similarity

The RCM shape can be interpreted as follows: The value of $R_{\hat{c},\hat{p}}(c,p)$ contains the information on how much of the total attenuation measured at $(\hat{c},\hat{p})$ appears in the value measured at (c,p). Due to this property, the neighboring RCMs are very similar in regions where the dominant structures are very similar, so it can be used as a basis for the SAS filter kernel. For locations where local structures differ, the similarity between RCMs decreases and major contributions from other dominant structures may prevent strong smoothing in these directions. The averaging between these values has to be blocked. As the RCM is a measure for the local structure, it is perfectly suited to detect those structural changes. We can determine the structural similarity $s_{\hat{c},\hat{p}}(\hat{c}',\hat{p}')$ between neighboring measurement values at $(\hat{c},\hat{p})$ and $(\hat{c}',\hat{p}')$ by comparison of the RCMs at both locations.

The structural similarity $s_{\hat{c},\hat{p}}(\hat{c}',\hat{p}')$ can be calculated from the RCMs in various ways by employing any similarity or correlation measure on pairs of RCMs. The following variant describes a very simple approach using the sum of absolute differences as a dissimilarity measure:

$$\hat{s}_{\hat{c},\hat{p}}(\hat{c}',\hat{p}') = \sum_{\hat{c}''}\sum_{\hat{p}''} \left\{ \left| R_{\hat{c},\hat{p}}(\hat{c}'',\hat{p}'') - R_{\hat{c}',\hat{p}'}(\hat{c}''-\hat{c}',\hat{p}''-\hat{p}') \right| \right\} \tag{8}$$

The expression $\hat{s}_{\hat{c},\hat{r}}(\hat{c}',\hat{r}')$ actually yields a non-normalized dissimilarity by computing the shifted difference of the two RCMs. We normalize this measure and convert it to a similarity measure by computing:

$$s_{\hat{c},\hat{p}}(\hat{c}',\hat{p}') = 1 - \frac{\hat{s}_{\hat{c},\hat{p}}(\hat{c}',\hat{p}')}{\sum_{\hat{c}'}\sum_{\hat{p}'} \hat{s}_{\hat{c},\hat{p}}(\hat{c}',\hat{p}')} \tag{9}$$

with $s_{\hat{c},\hat{p}}(\hat{c}',\hat{p}') \in [0,1]$, pairs of measurement values with an equal RCM-structure get an $s_{\hat{c},\hat{p}}(\hat{c}',\hat{p}')$-value of 1.

D. SAS Filter Calculation

With the similarities $s_{\hat{c},\hat{p}}(\hat{c}',\hat{p}')$ we can compute the final local filter $f_{\hat{c},\hat{p}}(\hat{c}',\hat{p}')$ by constructing a bilateral filter-type kernel using a spatial neighborhood filtering component and the structural neighborhood component of Eq. (9).

Note that it is theoretically possible to construct filter kernels with a range of more than one projection. However, this can make the filter prone to produce artifacts at high contrast objects since filtering over projections tends to cause minor inconsistencies in the data. Therefore we provide a 1-D kernel which performs filtering only within one projection. It is a univariate Normal distribution with extends in channel direction:

$$\mathcal{N}^{(\sigma^2)}_{\hat{c},\hat{p}}(\hat{c}',\hat{p}') = \frac{1}{\sqrt{2\pi}\sigma} \cdot \exp\left\{ \frac{(\hat{c}'-\hat{c})^2}{\sigma^2} \right\} \tag{10}$$

Its mean value is placed at the center position of the filter $\hat{c},\hat{p}$ and σ should be linked to $\Delta p_{\max}$ so that contributions beyond this range are negligible. Thus, only $\Delta p_{\max}$ steers the overall filter strength. The resulting local filter kernel is the normalized product of the spatial and structural similarity term

$$\tilde{f}_{\hat{c},\hat{p}}(\hat{c}',\hat{p}') = s_{\hat{c},\hat{p}}(\hat{c}',\hat{p}') \cdot \mathcal{N}^{(\sigma^2)}_{\hat{c},\hat{p}}(\hat{c}',\hat{p}'). \tag{11}$$

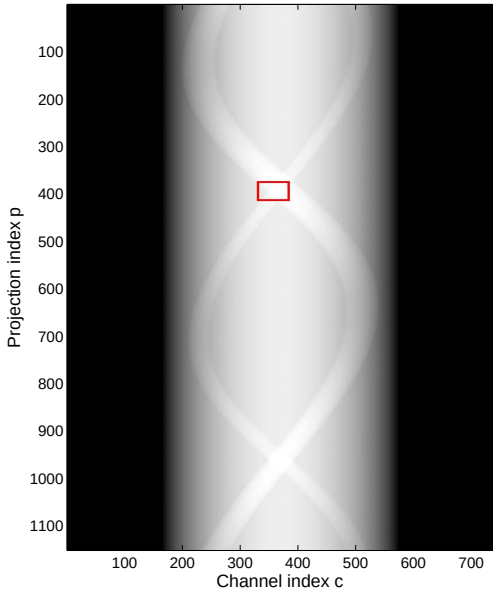

(a) Example sinogram (box indicates the magnified excerpt of Fig. (b)).

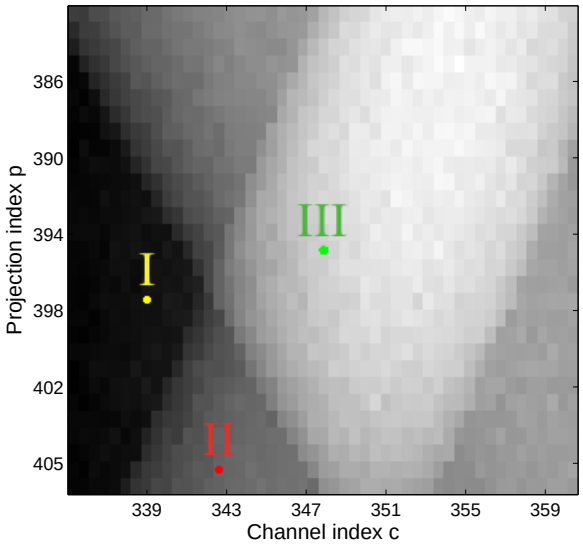

(b) Excerpt with marked sample measurements.

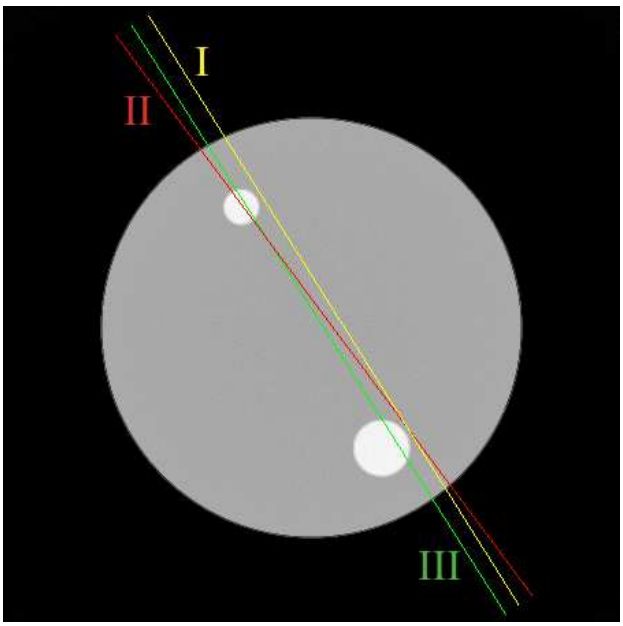

(c) Reconstructed slice with corresponding measurement lines.

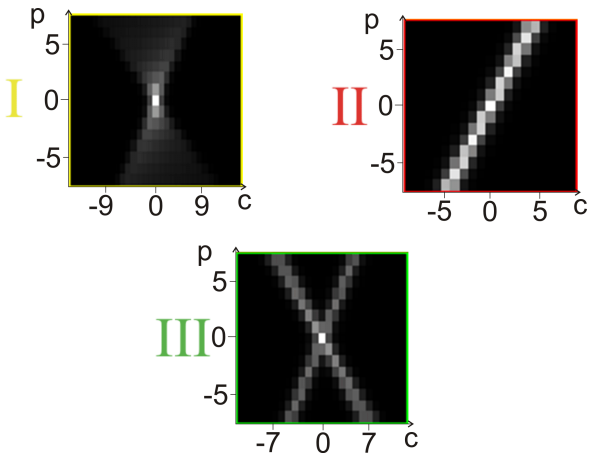

(d) RCMs.

Fig. 4. Example for correspondences between projection and object space: (a) shows a sinogram of a simple phantom (Intensity window center (c): 5.25, width (w): 10.5, no unit), (b) shows a magnified excerpt with markers at sample locations, (c) shows the reconstructed slice (c: -250 HU, w: 1500 HU) with the ray lines in corresponding colors to the markers of Fig. (b) and Fig. (d) shows the RCMs for the measurement lines (Roman numerals indicate the correspondences, HU is Hounsfield units).

$$f_{\hat{c},\hat{p}}(\hat{c}',\hat{p}') = \frac{\tilde{f}_{\hat{c},\hat{p}}(\hat{c}',\hat{p}')}{\sqrt{\sum_{\hat{c}'}\sum_{\hat{p}'}\tilde{f}_{\hat{c},\hat{p}}(\hat{c}',\hat{p}')^2}} \tag{12}$$

The normalized similarity masks $f_{\hat{c},\hat{p}}(\hat{c}',\hat{p}')$ for the sample locations shown in Fig. 4b are depicted in Fig. 6. These images demonstrate the basic properties of the filter: In homogeneous regions, the shape of the RCMs is similar and a high structural similarity causes strong smoothing into these directions. At borders with changing the local structure, no smoothing takes place and edges are preserved. This ensures strong noise reduction by an automatically steered averaging according to the similarity of the measured values.

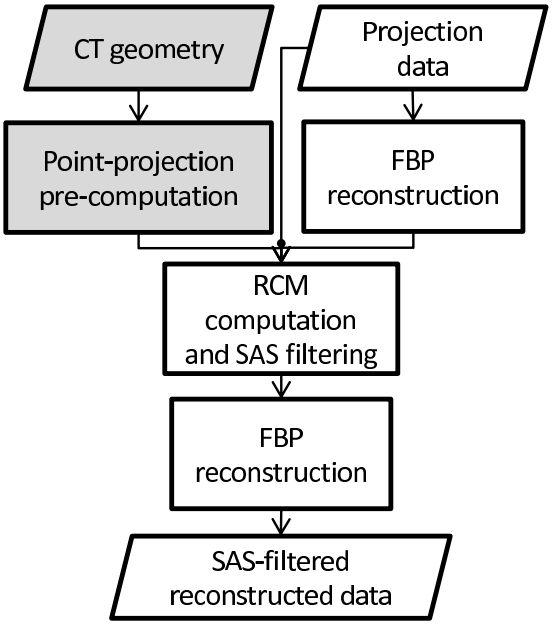

Fig. 5. Schematics of the SAS-filter data flow. Static data and pre-computation steps are marked gray.

This approach fulfills the requirement stated above: Maximal smoothing between values with similar local structures according to their common attenuation and smoothing over values with different local structures is blocked. The structures are not estimated in the projection domain but from a projection model.

E. Adaptive Filter Range

The RCM-similarity can also be used to perform a dynamic, homogeneity-driven range adaption. This measure is used to reduce the overall filter influence in regions with large structural inhomogeneity or transitions between different dominating local structures. In practice, it has a positive influence on the overall image quality of the RCM filter results. We choose a very simple homogeneity adaption which incorporates the required properties. It scales the standard deviation σ of the spatial filter component defined in Eq. (10) with a homogeneity term. For the filter kernel of Eqs. (11) and (12) with a filter range of one projection and $\Delta p_{\max}$ channels, the scaling factor is defined as follows:

$$h_{\hat{c},\hat{p}} = \sum_{\hat{c}'=\hat{c}-\Delta p_{\max}/2}^{\hat{c}+\Delta p_{\max}/2} s_{\hat{c},\hat{p}}(\hat{c}',\hat{p}')/\Delta p_{\max}. \tag{13}$$

i. e. σ is replaced with $\sigma \cdot h_{\hat{c},\hat{p}}$. In case of total structural homogeneity in the neighborhood of $(\hat{c},\hat{p})$, $h_{\hat{c},\hat{p}} = 1$ and no size adaption is performed. With increasing inhomogeneity, $h_{\hat{c},\hat{p}}$ decreases and thus the filter range is decreased which reduces the overall filter strength. This can be combined with a noise model-driven filter range adaption.

III. Materials and Methods

A. Implementation Details

Our implementation of $\mathcal{P}_{\mathrm{P}}(\mathbf{r},\bar{\mu}(\mathbf{r}))$ features a pin-hole projection model and a numerical temporal integration for the sampling of the projection angles. The beam profile was assumed to follow a Normal distribution. The FWHM of the Normal distribution at the tube focus point was set to 0.9 mm in all evaluations. The used detector sizes were 678 or 736 channels and 1152 projections per rotation were acquired. In the measured data a detector quarter channel offset and an indirect fan-beam reconstruction was used. In simulations, no quarter offset was assumed and a direct fan-beam reconstruction was used. In most experiments, the pre-reconstruction and the final reconstruction both were performed with a Ram-Lak or a Shepp-Logan reconstruction kernel. Other kernel combinations are explicitly mentioned. Figure 5 visualizes the data flow for a complete SAS-filtered reconstruction.

B. Optimization

Some essential optimizations have to be performed for a practical implementation of the algorithm. A naive realization of the formulas presented above would require a huge amount of computations. The resulting computation time would render the filtering impractical. Fortunately, the computation can be reformulated to exploit symmetries and enable a pre-computation of intermediate results that only depend on the system geometry and not on the imaged object. These computations have to be performed only once for a fixed scanner set-up and may be reused for each scan. They may include measurement effects like the temporal integration of projections during one projection.

The pre-computation makes use of the fact that the shape of all point-based forward projections does not depend on the absolute projection angle. The point-based analytic projections can be very expensive operations, so we want to ensure that as little projections as possible are computed and that no projections have to be computed during the filtering phases. It is sufficient to compute all forward projections for a single projection. These forward projections can be stored and re-used for further filter computations as only the scale of the projections depends on the actual data whereas the shape is fully dependent on the scanner geometry. So the first step of the optimized algorithm is the pre-computation phase, where all sample locations on all rays of the X-ray fan for a fixed

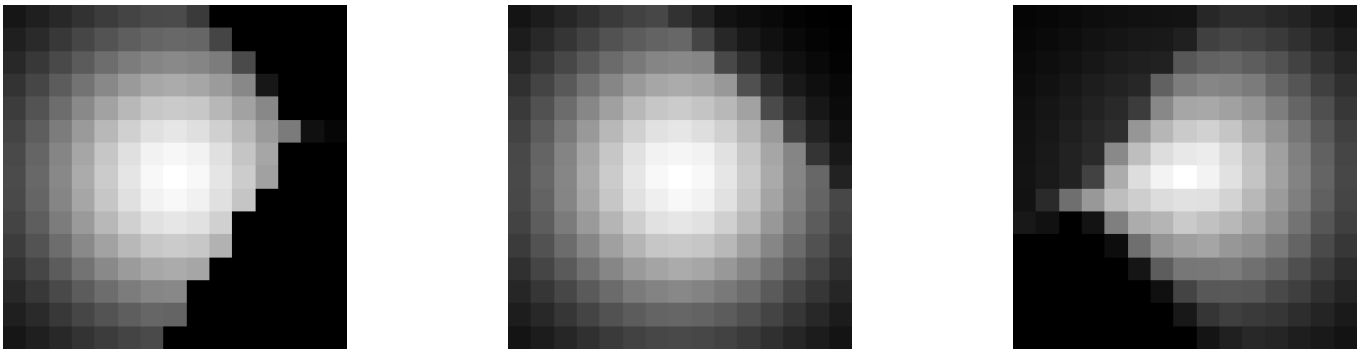

(a) I (b) II (c) III

Fig. 6. Normalized RCM similarity masks for the examples given in Fig. 4. The Roman numerals indicate the correspondence with the markers in Fig. 4b and the lines in Fig. 4c. The center line corresponds to the shape of the filter kernels with a range of one projection.

projection angle are determined. For each sample, the point-based forward projections (Eq. 1) are computed for a neutral local attenuation value $\bar{\mu}(\mathbf{r})$ of one.

The filtering itself involves the following steps: First of all, a pre-reconstruction with a sharp filter kernel has to be performed. It is used for the RCM computation of Eq. (7): One RCM corresponds to one sampled ray path. The ray path has to be rotated according to the projection angle, then the pre-reconstructed slice is interpolated at the according sample locations, the main contributions are identified and a weighted addition of the according pre-computed projection masks is performed. The interpolated values of $\bar{\mu}(\mathbf{r})$ are used as weights. The result of this operation is one RCM for each channel and projection which are held in memory for the next step.

The filter computation step of Eq. (11) can be carried out in a straight-forward fashion. The required similarity measures of Eqs. (8) and (9) can be computed on demand from the RCMs from the previous steps. A re-usage of similarity values computed earlier in the filter computation phase is unlikely to bring significant advantages as due to the storage and organization overhead.

The application of the filter is the final step. The filter changes for every sinogram location. This property leaves little room for high-level optimization, but the computational costs of these steps are negligible.

The overall complexity is dominated by the RCM computation. It scales linearly with the product channels $\times$ projections $\times$ samples per ray.

C. Phantoms and Experiments

Four different phantom set-ups were used for the performance evaluations (Tab. I): The first (A) one consists of a CT-scan of a high resolution phantom of aluminum insets in PMMA (Catphan HR[1], see Fig. 7a). It was used to assess noise and sharpness of the SAS filter.

Set-up B involves in vivo CT-scans of live patients. In order to visually assess the influence of this filter on image data, we use several patient data sets acquired with a Siemens SOMATOM Definition (Siemens AG, Forchheim, Germany). All scans were conducted at $140\,\mathrm{kVp}$ tube voltage, $1.2\,\mathrm{mm}$ slice width, no flying focal spot. The integration time was set to $433\,\mu\mathrm{s}$ at a rotation time of $0.5\,\mathrm{s}$. The selected tube currents were in the range of $55\,\mathrm{mA}$ to $80\,\mathrm{mA}$.

[1]Catphan 500, *http://www.phantomlab.com/catphan.html*, The Phantom Laboratory, Salem, NY, USA

	Object	Type	Evaluated quantities
A	Catphan HR phantom	measured	MTF, noise, artifacts
B	Patient data	measured	Noise, visual image quality
C	Complex phantom	simulated	Noise, MTF
D	Low contrast inset in water	simulated	MTF, noise

TABLE I
OVERVIEW OF CONDUCTED EXPERIMENTS.

In some experiments, a Shepp-Logan kernel was used for pre- or final reconstruction instead of a Ram-Lak kernel. Here, the reconstruction quality for realistic application scenarios and the visual influence of filter parameters was inspected and compared to a standard FBP with adapted reconstruction kernel and a standard bilateral filter result. The filter parameter of the FBP reconstruction and the bilateral filter where adjusted so that an approximately similar overall noise standard deviation was achieved. The standard deviation of voxel values in homogeneous tissue regions of the reconstructed images were taken as an estimate for the image noise. The FBP kernels are referred to as Cos*XXX* kernels where *XXX* stands for a two or three digit number indicating the cut-off frequency f_c relative to the Nyquist frequency f_N. Cos50 represents a kernel with a cut-off frequency at $50\,\%$ of the Nyquist frequency, Cos675 means $f_\mathrm{c} = 0.675 \cdot f_\mathrm{N}$.

The calculation rule for the discrete filter of length l samples is as follows:

$$K(i) = K(l-i-1) = \frac{i}{l} \cdot \frac{\pi}{N_\mathrm{r}} \cos\left(\frac{\pi \cdot i}{i_\mathrm{c}}\right) \qquad (14)$$

for $\left\{i \in \mathbb{N} | 0 \leq i < \frac{1}{2} \cdot l\right\}$. The cut-off index is defined as $i_c = l \cdot \frac{f_c}{f_\mathrm{N}}$ and N_r is the number of projections per rotation. The bilateral filter was chosen to have roughly the same spatial extent as the SAS filter and the photometric similarity parameter was selected in a way that the estimated noise

amplitude matches the other two results.

The purpose of set-up C is a quantitative performance comparison of the SAS filter and a standard bilateral filter. We conducted 1000 simulations and reconstruction of an anthropomorphic, simulated phantom with complex structures (Fig. 8a). The large number of repetitions was chosen so that the filtered images could be averaged to eliminate noise-influences and the MTF curves only contain frequencies of the noise-free averaged signal. The filter strengths were again chosen to have the same spatial extent and exact same SNR gain. We used an signal amplitude over noise standard deviation as SNR definition. Here we compare the edge MTF [26] on the edge of a elliptic contrast probe placed in the phantom. Higher MTF values indicate that the filter sacrifices less image sharpness for reducing the image noise.

Scenario D also uses simulated data. Here we evaluate the edge MTF for varying CNR levels on a cylindrical water phantom with a circular inset of varying densities was simulated with an analytic forward projector for four different contrasts between inset and water (see Fig. 7b). For each contrast, 250 to 1000 scans were simulated and the filter was applied (the lowest contrasts required 500 resp. 1000 scans due to the low CNR). The edge between inset and water was used for an MTF estimation.

(a) Measured Catphan HR phantom.

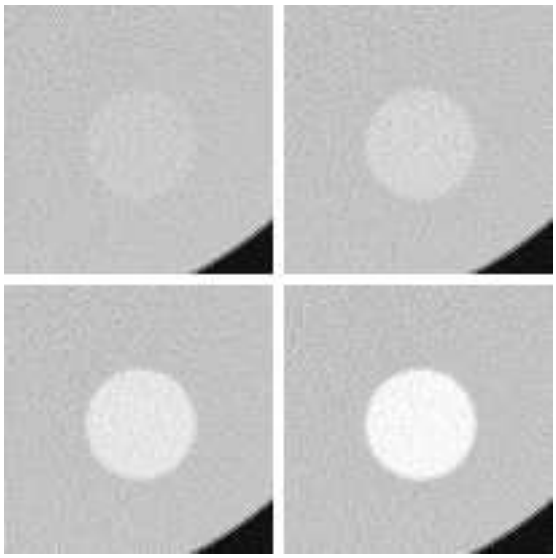

(b) Contrast insets in cylindrical water phantom.

Fig. 7. Phantoms used for evaluation. Figure (a) shows the Catphan High Resolution phantom with aluminum insets in PMMA (c: 346 HU, w: 2751 HU). The distances between insets ranges from 1 lp/cm to 21 lp/cm. Figure (b) shows the four different contrast insets in a water phantom used for edge MTF evaluation (c: -387 HU, w: 1655 HU). The noise standard deviation is approx. 43 HU and the contrasts are 55 HU, 109 HU, 213 HU and 315 HU.

IV. Evaluation and Results

A. High Resolution Phantom

Figure 9 shows the MTF estimates for the standard FBP and an SAS filtered version. We can see only marginal changes in terms of relative contrast throughout the whole frequency range. This is due to the fact that the introduced filter clearly identifies the high-contrast structures throughout the whole sinogram and adapts the filters appropriately. No averaging takes place between components containing structure and background. In this case, the image sharpness is not affected and no additional reconstruction artifacts can be detected. The SAS filter manages to achieve a noise reduction of about 13.6 % from a standard deviation 10.3 HU without filter to 8.9 HU with filter (SNR increased from 97.0 to 112.3). Due to its many small high-contrast inlays this phantom can be considered as a benchmark for robustness against reconstruction artifacts.

B. Patient Data

Figures 10 and 11 show comparisons between standard FBP reconstructions, a standard bilateral filtered and SAS-filtered reconstructions of two different patient scans. Although the estimated noise amplitudes are approximately similar in Figs. 10b, 10c and 10d resp. 11a, 11b and 11c, the SAS filter causes visibly less blurring, especially at edges with higher CNR and high frequency components, for instance, the organ tissue textures are preserved better. At very high CNR edges, like the transition between air and tissue, the SAS filter can cause a minor amplification of the edge strength. At these edges, the standard bilateral filter also preserves the image sharpness. In the example of Fig. 10, the standard bilateral filter manages to preserve at least some of the structure but a decrease in sharpness is well visible compared to the SAS result. In Fig. 11, more complex structures are contained and the Bilateral filter fails to detect and preserve the most of the structure and causes strong visible blurring. The noise shaping characteristics are also very different: The cosine kernel attenuates high frequency noise components very strongly whereas low frequency noise passes the filter, consequently the noise grains are rather big and smooth. The noise in the SAS filter result (Fig. 10d) has a different frequency distribution which resembles the original noise structure more closely. The noise reduction is more homogeneous throughout the whole frequency range. Regarding this property, the result of the standard bilateral filter ranges in between Cosine-kernel and SAS filter result.

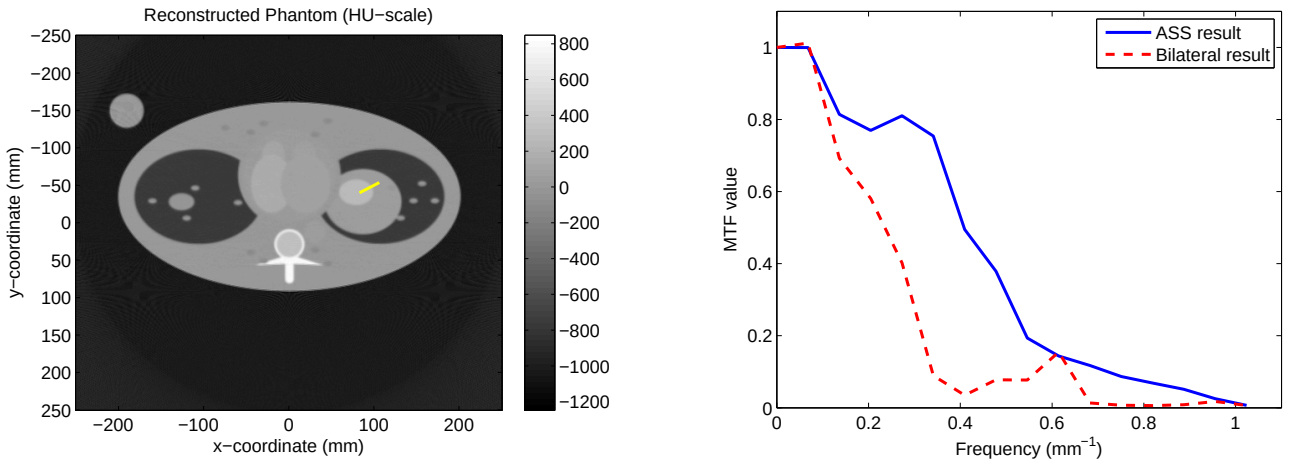

(a) Simulated phantom slice. (b) MTF comparison result.

Fig. 8. Evaluation set-up C: The line in (a) marks the location on which the edge MTF evaluation was performed.

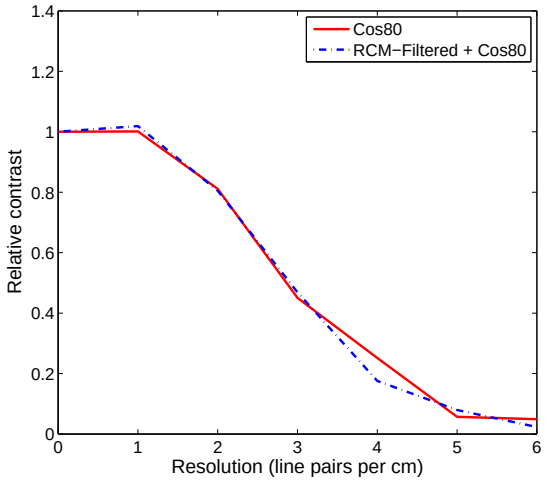

Fig. 9. Relative contrast of a standard reconstruction between insets and background for various line resolutions. Cos80 indicates a cosine reconstruction kernel with a cut-off frequency at 80 % of the detector Nyquist frequency.

The noise shaping characteristics can be influenced by altering the filter parameters. In general, the noise shaping characteristics of SAS filtering are less intuitively linked to the filter parameters than for standard reconstruction kernels. However, a desired specific noise shaping characteristic can be achieved by adapting the filter kernel of the final reconstruction of the SAS filter result. For instance, a smoother post-reconstruction kernel leads to stronger smoothing of the SAS filter result. A smoother pre-reconstruction filter also influences the SAS filter. This property is visualized in Fig. 11d. Here we investigate the influence of the pre-reconstruction kernel. We used a Shepp-Logan kernel instead of a Ram-Lak kernel for the pre-reconstruction. This leads to a visible decrease in sharpness and noise, however the sharpness is still better than for the standard bilateral filter result (Fig.11c). The amount of noise reduction of approx. 12 % corresponds to the noise amplitude of a standard FBP with a Cos525 kernel (SNR increases from 33.0 to 37.5). This indicates that the pre-reconstruction kernel has a clearly visible influence on the SAS filtering result and can be used to influence the filter properties of the SAS filter.

C. MTF Comparison Between Bilateral and SAS Filter

This experiment provides a quantitative verification of the findings from set-up B. Figure 8b shows the edge MTF extracted from the 1000 realizations. The overall SNR in homogeneous soft tissue part of the phantom was increased almost equally for both filters from 47.8 to 98.9 (bilateral) resp. 105.5 (SAS). The MTF evaluation shows that the standard bilateral filters fails to preserve the edge sharpness as it cannot distinguish the structures in the projection data. It basically degrades to a low-pass filter and reaches the noise reconstruction goal by sacrificing image sharpness. This results in blurring the edges of the structure and leads to a reduction of the higher frequencies in the MTF curve. The SAS filter mostly blocks smoothing across the the borders of the structure's trace in the sinogram space and consequently its edge MTF has higher values throughout the whole mid and high frequency range. It sacrifices much less sharpness to reach the same noise reduction performance. The small peak in the MTF of the bilateral filter at $0.6\,mm^{-1}$ can most likely be attributed to a very small reconstruction artifact which appeared systematically in the bilateral filter results, however, neither method caused a considerable increase in reconstruction artifacts compared to the standard reconstruction without non-linear filtering. This corresponds to the visual impression of the image sharpness in the patient images of set-up B. The sharpness gain of the SAS method can be sacrificed for dose reduction by choosing a softer reconstruction kernel as shown in Fig. 11.

D. Noise Reduction and MTF for varying contrasts

This evaluation addresses the frequency transfer behavior of the SAS filter. This is done by measuring the image MTF

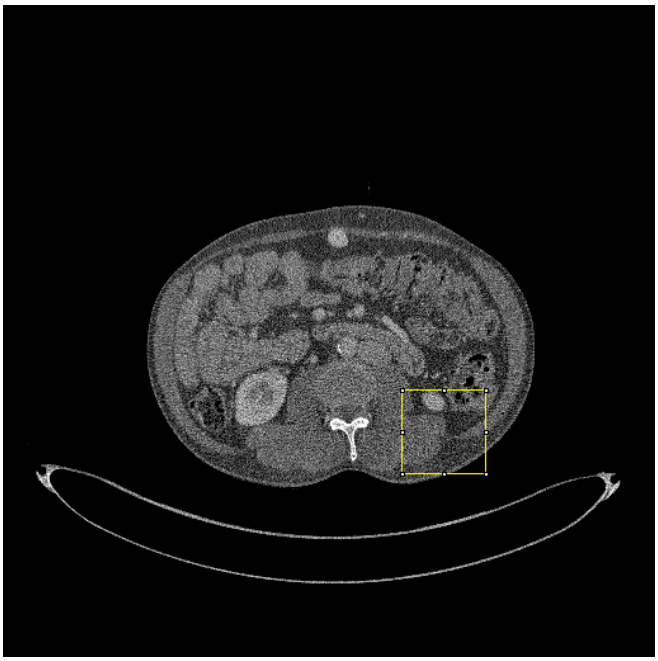

(a) Reconstructed slice.

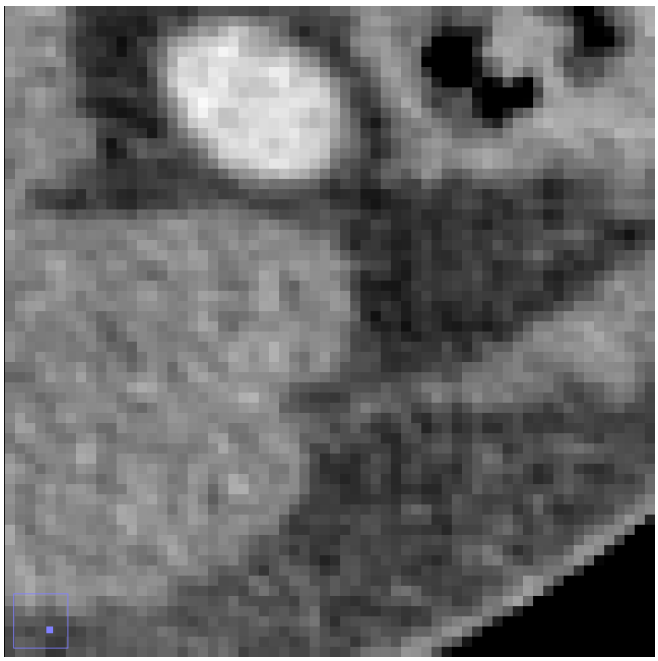

(b) Cos625 reconstruction.

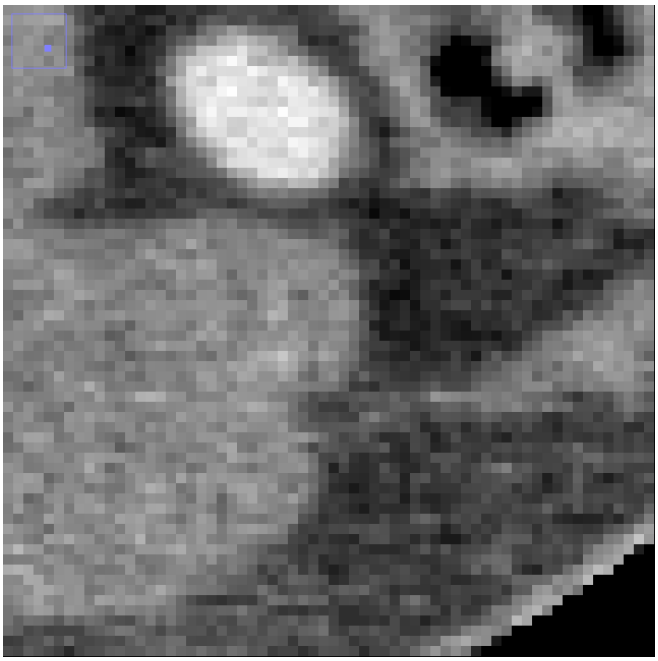

(c) Standard bilateral filter reconstruction.

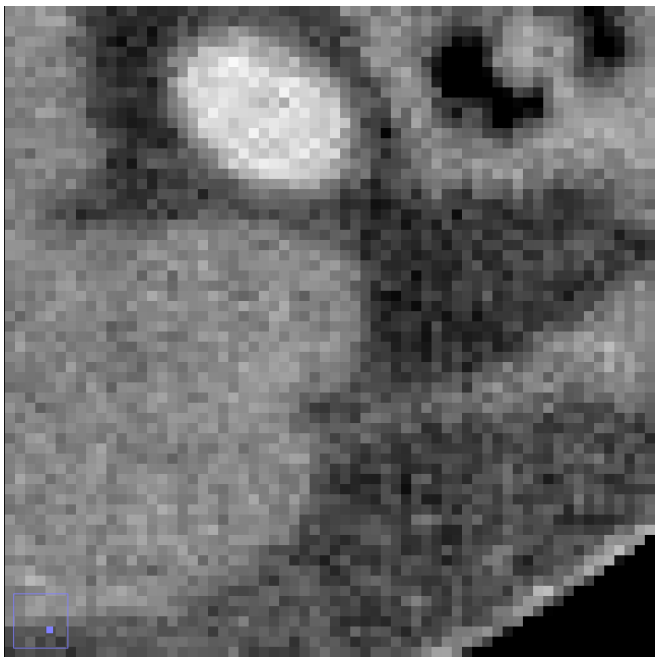

(d) SAS result.

Fig. 10. Filter results for first patient dataset: (a) Ram-Lak reconstruction of the data-set used as input image for the SAS filter, (b) magnified excerpt (Cos625 kernel), (c) result of the standard bilateral filter and (d) result of the SAS filter (9×9 RCM size, 0.225 smoothing, structure preservation 0.9, homogeneity adaption on). The water scaling was omitted in these tests, so no intensity windows are given. Original images are a courtesy of Prof. Dr. Andreas H. Mahnken, RWTH Aachen, Germany. The box in (a) marks the region where the excerpts shown in (b)-(d) were taken.

(a) Cos575 reconstruction.

(b) RCM result.

(c) Standard bilateral filter reconstruction.

(d) RCM with Shepp-Logan pre-reconstruction.

Fig. 11. Filter results for second patient dataset: (a) Magnified excerpt (Cos575 kernel), and (b) result of the RCM filter (9×9 RCM size, 0.5 smoothing, structure preservation 0.8, homogeneity adaption on), (c) bilateral filter result and (d) result with Shepp-Logan filtered pre-reconstruction. Original images are a courtesy of Prof. Dr. Andreas H. Mahnken, RWTH Aachen, Germany.

Contrast	Std. dev. original	Std. dev. filtered	Noise Reduction
55 HU	27.7 HU	3.87 HU	86.0 %
109 HU	33.2 HU	5.75 HU	82.7 %
213 HU	33.2 HU	6.40 HU	80.7 %
315 HU	33.2 HU	6.54 HU	80.3 %

TABLE II
ESTIMATED NOISE REDUCTION FOR VARIOUS CONTRASTS.

of a standard Ram-Lak filtered FBP and an SAS filtered reconstruction on an edge phantom. We chose 250 to 1000 repetitions depending on the examined CNR level.

Figure 12 shows the resulting azimuthal edge MTFs for four different contrasts. The noise standard deviations in the Ram-Lak filtered original and the processed versions are given in Tab. II. For the 55 HU low contrast case we can observe a slight reduction of the MTF in the mid-frequency range, in the 109 HU case, the MTFs are very similar between original and filtered case. The two higher contrast cases show a slightly edge enhancing property of the filter at higher frequencies whereas low frequencies are attenuated slightly. This reveals the frequency transmission behavior of the projection filter when it is fully adapted to the edge shape in the sinogram. This causes the edge to be visibly enhanced in the filtered sinogram. The total noise reduction achieved for these examples is shown in Tab. II. It shows the standard deviation of the noise for a Ram-Lak reconstruction and the RCM filtered reconstruction. In this simplified scenario a very strong noise reduction of over 80 % can be achieved. More dominant structures slightly reduce the total noise reduction. This can be seen in the standard deviations of the 109 HU to 315 HU cases. In the 55 HU case, we used a cosine reconstruction kernel for the pre-reconstruction, therefore the noise in the original images is already slightly lower. However, the relative noise reduction agrees with the other cases.

E. Complexity, Run-Time and Performance

All computations were carried out on a standard desktop computer equipped with an Intel Core i7 860 CPU at 2.8 GHz and 8 GB of DDR3 RAM. The filter computation consists of three phases: The initialization of the forward projections, the RCM computation and the filter generation and application. All these steps depend on the desired filter size in projections which was kept constant at 5 throughout all experiments. The time for the pre-computation of the forward projections depends on the number of detector channels, the ray sampling distance and the complexity of the point-based forward projector model. Unlike the following two phases it can be pre-computed for a given geometry as it does not depend on the imaged object. So the computation time of this phase does not add to the filter time. Our reference implementation with 736 detector channels and at sample distance of exactly one pixel width took about one minute for a $\Delta r_{\max}$-value of 9. The RCM computation depends on the number of channels, projections, ray sampling distance and $\Delta p_{\max}$. This phase took our reference implementation between 20 seconds to 1 minute, whereas the filter generation and application phase depends only on the number of channels and projections and required about two to three seconds on average. This leads to a filter times of approx. 1 minute per slice. Additionally the pre-reconstruction and the reconstruction of the SAS result have to be carried out. The computation time from sinogram to reconstructed and filtered slice totals to about 2 minutes per slice. The memory consumption is dominated by the size of the pre-computed point-based projection table and the RCM table. Not all tables have to reside in memory completely. Since the sizes are usually not critical on current hardware, we did no optimizations regarding this issue. It our set-up the pre-computed table size is approx. 100 MB, the peak memory consumption is about 4 to 8 GB for eight parallel threads.

V. CONCLUSIONS

The RCM-based SAS filter presented in this paper is a novel approach to structure-preserving spatial filtering in projection data. We showed that this approach can detect and preserve structures in the projection domain while making use of the good contrast in the reconstructed data. The filter properties were assessed on measured and simulated phantom data as well as measured patient data. The patient data tests showed that image sharpness is superior to a standard FBP reconstruction and a bilateral filter result with the same total noise. The image MTF and high-frequency texture is well preserved even for low contrasts. A test on a simulated complex phantom showed that SAS is able to detect and preserve structures in projection space that are blurred by a standard bilateral filter with the same noise reduction potential. The noise reduction in a simple edge phantom case exceeded 80 %, in scenarios with complex structure, a noise reduction of approx. 15 % is estimated for similarly sharp results. We also demonstrated that the filter can deal with structures that are prone to cause reconstruction artifacts. The modulation transfer behavior of the filter was evaluated on simulated phantom data. The filter MTF is contrast dependent. For small contrasts around 50 HU, a reduction of the mid-frequencies can be observed, for higher contrasts it follows the original MTF closely and tends to enhance higher frequencies and attenuate low- and mid-frequencies in the reconstructed image.

REFERENCES

[1] M. Hilts and C. Duzenli, "Image noise in X-ray CT polymer gel dosimetry," *Journal of Physics Conference Series*, vol. 3, pp. 252–256, 2004.

[2] H. Gress, H. Wolf, U. Baum, M. Lell, M. Pirkl, W. Kalender, and W. Bautz, "Dose reduction in computed tomography by attenuation based on-line modulation of tube current: Evaluation of six anatomical regions," *European Radiology*, vol. 10, no. 2, pp. 391–394, 2000.

[3] N. Mail, D. J. Moseley, J. H. Siewerdsen, and D. A. Jaffray, "The influence of bowtie filtration on cone-beam CT image quality," *Medical Physics*, vol. 36, no. 1, pp. 22–32, 2009. [Online]. Available: http://link.aip.org/link/?MPH/36/22/1

[4] A. Rose, "A unified approach to the performance of photographic film, television pickup tubes and the human eye," *J. Soc. Motion Pict. Eng.*, vol. 47, p. 273, 1946.

[5] H. J. Zwieg, "Detective quantum efficiency of photodetectors with some amplifying mechanism," *Journal of the Optical Society of America*, vol. 55, pp. 525–528, 1965.

[6] M. Rabbani, R. Shaw, and R. V. Metter, "Detective quantum efficiency of imaging systems with amplifying and scattering mechanisms," *J. Opt. Soc. Am. A*, vol. 4, no. 5, pp. 895–901, 1987. [Online]. Available: http://josaa.osa.org/abstract.cfm?URI=josaa-4-5-895

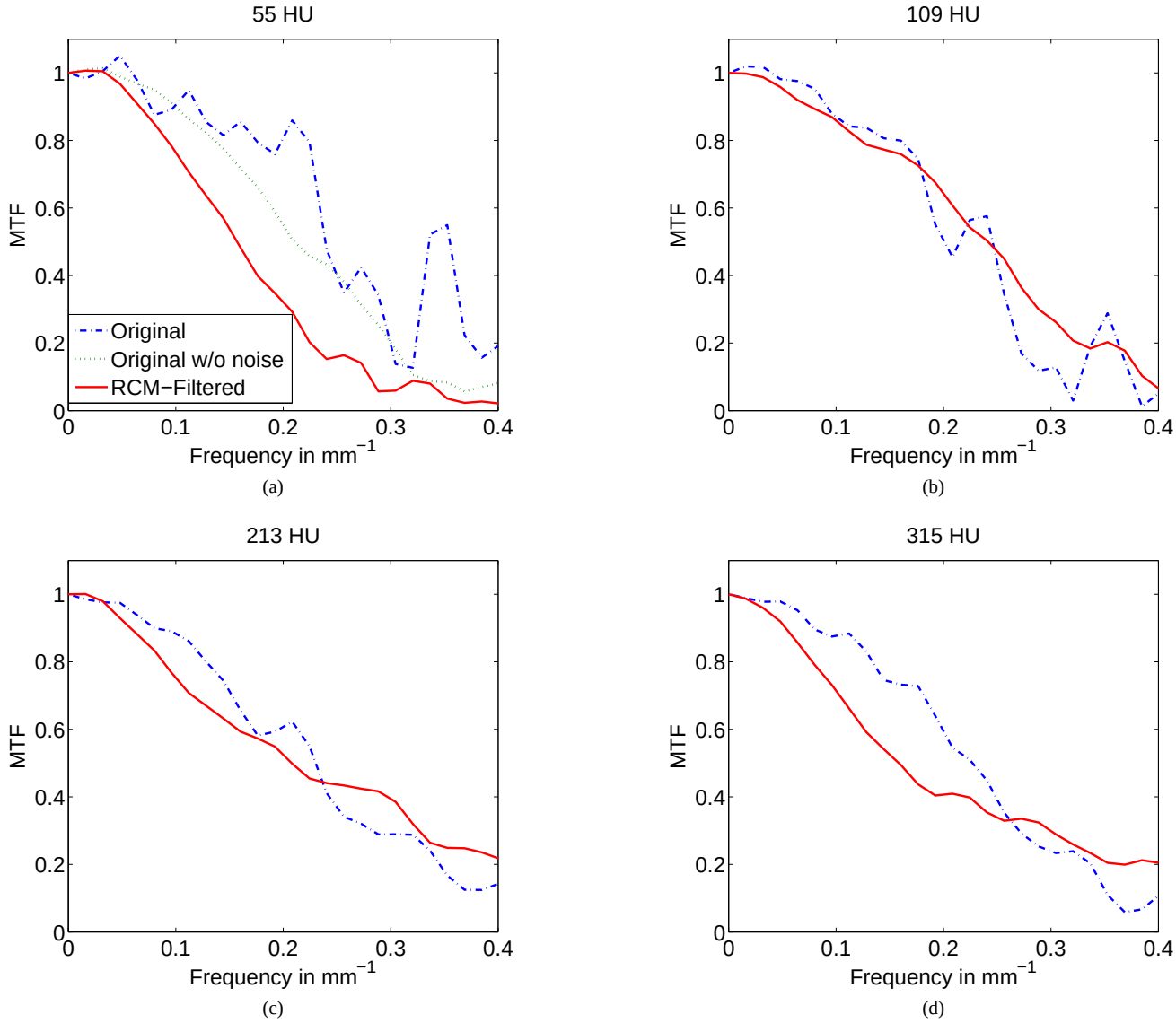

Fig. 12. MTF comparisons for varying contrast strengths of insets. For the 55 HU example, 1000 realizations were simulated and the MTF estimate from a noise-free unfiltered realization is also shown. For the 109 HU case 500 realizations and for the other examples 250 realizations each were simulated. The estimates from the noise-free realization are omitted for the last three cases as there is only a minor influence of the noise for this number of realizations.

[7] I. A. Cunningham and R. Shaw, "Signal-to-noise optimization of medical imaging systems," *Journal of the Optical Society of America A*, vol. 16, no. 3, pp. 621–632, 1999. [Online]. Available: http://josaa.osa.org/abstract.cfm?URI=josaa-16-3-621

[8] L. A. Feldkamp, L. C. Davis, and J. W. Kress, "Practical cone-beam algorithm," *Journal of the Optical Society of America A*, vol. 1, no. 6, pp. 612–619, 1984.

[9] A. C. Kak and M. Slaney, *Principles of Computerized Tomographic Imaging*. Society of Industrial and Applied Mathematics, 2001.

[10] E. Chew, G. H. Weiss, R. A. Brooks, and G. Di Chiro, "Effect of CT Noise on Detectability of Test Objects," *American Journal of Radiology*, vol. 131, pp. 681–685, 1978.

[11] J. Hsieh, "Adaptive streak artifact reduction in computed tomography resulting from excessive x-ray photon noise," *Medical Physics*, vol. 25, no. 11, pp. 2139–2147, 1998.

[12] M. Kachelriess, O. Watzke, and W. A. Kalender, "Generalized multi-dimensional adaptive filtering for conventional and spiral single-slice, multi-slice, and cone-beam CT," *Medical Physics*, vol. 28, no. 4, pp. 475–490, 2001.

[13] A. Borsdorf, R. Raupach, T. Flohr, and J. Hornegger, "Wavelet based Noise Reduction in CT-Images using Correlation Analysis," *IEEE Transactions on Medical Imaging*, vol. 27, no. 12, pp. 1685–1703, 2008.

[14] T. Flohr, C. McCollough, H. Bruder, M. Petersilka, K. Gruber, C. Süß, M. Grasruck, K. Stierstorfer, B. Krauss, R. Raupach, A. Primak, A. Kttner, S. Achenbach, C. Becker, A. Kopp, and B. Ohnesorge, "First performance evaluation of a dual-source CT (DSCT) system," *European Radiology*, vol. 16, pp. 256–268, 2006.

[15] F. Catte, P.-L. Lions, J.-M. Morel, and T. Coll, "Image selective smoothing and edge-detection by nonlinear diffusion," *SIAM Journal on Numerical Analysis*, vol. 29, pp. 182–193, 1992.

[16] J. Weickert, *Anisotropic Diffusion in Image Processing*. Stuttgart: Teubner-Verlag, 1998.

[17] J. Wang, H. Lu, T. Li, and Z. Liang, "Sinogram noise reduction for low-dose CT by statistics-based nonlinear filters," J. M. Fitzpatrick and J. M. Reinhardt, Eds., vol. 5747, no. 1. SPIE, 2005, pp. 2058–2066.

[18] M. Schaap, A. M. R. Schilham, K. J. Zuiderveld, M. Prokop, E.-J. Vonken, and W. J. Niessen, "Fast Noise Reduction in Computed Tomography for Improved 3-D Visualization," *IEEE Transactions on Medical Imaging*, vol. 27, no. 8, pp. 1120–1129, 2008.

[19] C. Tomasi and R. Manduchi, "Bilateral filtering for gray and color images," in *Sixth International Conference on Computer Vision*, 1998, pp. 839–846.

[20] A. Borsdorf, S. Kappler, R. Raupach, and J. Hornegger, "Analytic Noise Propagation for Anisotriopic Denoising of CT Images," in *2008*

IEEE Nuclear Science Symposium Conference Record, P. Sellin, Ed., 2008, pp. 5335–5338. [Online]. Available: http://www5.informatik.uni-erlangen.de/Forschung/Publikationen/2008/Borsdorf08-ANPb.pdf

[21] A. Manduca, L. Yu, J. D. Trzasko, N. Khaylova, J. M. Kofler, C. M. McCollough, and J. G. Fletcher, "Projection space denoising with bilateral filtering and CT noise modeling for dose reduction in CT," *Medical Physics*, vol. 36, pp. 4911–4919, 2009.

[22] S. Wirth, W. Metzger, K. Pham-Gia, and B. J. Heismann, "Impact of Photon Transport Properties on the Detection Efficiency of Scintillator Arrays," *IEEE Nuclear Science Symposium Conference*, no. M11-212, pp. 2602–2603, 2003.

[23] A. M. R. Schilham, B. van Ginneken, H. Gietema, and M. Prokop, "Local Noise Weighted Filtering for Emphysema Scoring of Low-Dose CT Images," *IEEE Transactions on Medical Imaging*, vol. 25, no. 4, pp. 451–463, 2006.

[24] H. Lu, X. Li, L. Li, D. Chen, Y. Xing, J. Hsieh, and Z. Liang, "Adaptive noise reduction toward low-dose computed tomography," in *Society of Photo-Optical Instrumentation Engineers (SPIE) Conference Series*, ser. Presented at the Society of Photo-Optical Instrumentation Engineers (SPIE) Conference, M. J. Yaffe and L. E. Antonuk, Eds., vol. 5030, June 2003, pp. 759–766.

[25] L. Keselbrener, Y. Shimoni, and S. Akselrod, "Nonlinear filters applied on computerized axial tomography: theory and phantom images," *Medical Physics*, vol. 19, pp. 1057–1064, July 1992.

[26] P. F. Judy, "The line spread function and modulation transfer function of a computed tomographic scanner," *Medical Physics*, vol. 3, no. 4, pp. 233–236, 1976. [Online]. Available: http://link.aip.org/link/?MPH/3/233/1